

# A steerable non-paraxial Gaussian beam expansion for a steerable parametric array loudspeaker

Tao Zhuang,<sup>1</sup>  Jiaxin Zhong,<sup>2,a)</sup>  Feng Niu,<sup>3</sup> Mahmoud Karimi,<sup>2</sup>  Ray Kirby,<sup>2</sup>  and Jing Lu<sup>1</sup> 

<sup>1</sup>Key Laboratory of Modern Acoustics and Institute of Acoustics, Nanjing University, Nanjing 210093, China

<sup>2</sup>Centre for Audio, Acoustic, and Vibration, University of Technology Sydney, New South Wales 2007, Australia

<sup>3</sup>Division of Mechanics and Acoustics, National Institute of Metrology, Beijing, China

## ABSTRACT:

A steerable parametric array loudspeaker (PAL) aims to steer a highly directional audio beam without the need to mechanically rotate the source. The Gaussian beam expansion (GBE) method is often used to model PALs because it is a computationally efficient approach, however the method relies on a paraxial approximation that can result in significant inaccuracies at large steering angles. To address this limitation, a steerable non-paraxial GBE is proposed in this article, where the mainlobe of the steered ultrasonic beam is included in the calculation by rotating the coordinate system. A non-paraxial approximation is then used to improve the accuracy of the method when integrating the virtual audio sources. The numerical results obtained using the proposed method are compared against those using the conventional GBE, as well as an exact solution. For a typical configuration, it is shown that for a conventional GBE the prediction error can be more than 30 dB at large angles, whereas the proposed method reduces this to less than 1 dB. The advantage of the proposed method is more significant at large steering angles, low audio frequencies, and those locations outside of the paraxial region. This improvement in performance is achieved with a computational cost that remains the same as the conventional GBE. © 2023 Acoustical Society of America.

<https://doi.org/10.1121/10.0016816>

(Received 14 September 2022; revised 6 December 2022; accepted 14 December 2022; published online 6 January 2023)

[Editor: Nickolas Vlahopoulos]

Pages: 124–136

## I. INTRODUCTION

Parametric array loudspeakers (PALs) generate highly directional audio sound using an ultrasonic carrier wave in air.<sup>1</sup> When a PAL radiates two harmonic ultrasound beams in air at different frequencies, the audio sound with the difference frequency is generated due to the second-order nonlinearity. The audio sound can be steered and focused by using the phased array technique.<sup>2,3</sup> A steerable PAL aims to steer the directional audio beam to the target direction without mechanically rotating the PAL.<sup>4</sup> Steerable PALs have been widely used in audio applications, such as active noise control,<sup>2,5</sup> local area vocalization,<sup>6</sup> and directivity control.<sup>4</sup>

A solution for the audio directivity of a PAL, termed “Westervelt directivity,” is often based on the collimating beam hypothesis and a paraxial approximation for the ultrasound was proposed first.<sup>1</sup> However, predictions are known to contain significant inaccuracies, and so attempts were made to improve the accuracy by including the directivities of ultrasonic waves, although predictions still deviate significantly from the experimental results.<sup>7,8</sup> Other models were also proposed to improve the accuracy including the advanced product directivity model and a convolution model.<sup>9–11</sup> Recently, an extended convolution model based on spectral analysis was proposed to compute the directivity of PAL when the ultrasound is amplitude-modulated.<sup>12</sup> However, predictions from

this and the aforementioned models are only valid in the far field, because the directivity model relies on a far field approximation to simplify computation.

To simulate the behavior of a PAL in the near field is more challenging because the general wave equation has a second-order nonlinearity in the near field.<sup>13</sup> In most cases, local effects are negligible at points that are not too close to the radiation surface,<sup>14</sup> which enables the wave equation to be simplified as Westervelt equation.<sup>13,15</sup> A quasilinear approximation can also be assumed because the ultrasound level generated by a PAL is usually limited in safety range,<sup>16</sup> which further simplifies the Westervelt equation.<sup>17</sup> Using this approach, the ultrasound pressure may be obtained using a twofold Rayleigh integral over the surface area of the PAL. An infinitely large volume source is then constructed with its source density proportional to the product of the ultrasound pressure. Finally, the audio sound is obtained using a threefold volume integral over the full space. This means that a fivefold integral is required, which is computationally expensive although the solution is exact in the whole space except at locations close to the PAL in the case of weak nonlinearity.<sup>14</sup> To reduce the computational cost of the quasilinear solution, a spherical expansion method was proposed.<sup>17</sup> By expressing the Green’s function as the superposition of spherical harmonics, the fivefold integral can be simplified by taking advantage of azimuthal symmetry. However, the spherical expansion method is only valid for a circular PAL with an axisymmetric excitation profile and is not applicable for a steerable PAL.

<sup>a)</sup>Electronic mail: jiaxin.zhong@student.uts.edu.au

The Gaussian beam expansion (GBE) method has been widely used to simplify the quasilinear solution.<sup>18,19</sup> This method approximates the vibration velocity on the PAL surface with the superposition of a set of Gaussian functions. The Rayleigh integral of ultrasound can then be simplified by using a paraxial approximation, which is expressed as a summation of Gaussian functions.<sup>20</sup> The virtual source density can be obtained after calculating the ultrasound by the GBE method. Finally, the volume integral of the virtual source is simplified by using a paraxial approximation.<sup>7</sup> The GBE method has been widely used to calculate the steering or focusing ultrasound generated by elliptical or rectangular radiators.<sup>21–23</sup> However, there are two problems associated with the GBE method: first, the on-axis prediction is inaccurate when the beam steering angle is beyond the paraxial approximation limitation (about 20°).<sup>22</sup> To overcome this issue, an improved GBE method was proposed by applying the linear phasing across each element of the array;<sup>24</sup> however, this means that the computational load scales with the number of array elements. Moreover, it is valid only for the linear radiation. Second, adopting a paraxial approximation can lead to large errors when computing the volume integrals at large steering angles and low audio frequencies.<sup>7</sup> To remove this limitation, a non-paraxial approximation for the Rayleigh integral computed for phased array transducers was proposed for the GBE method with the same level of computational complexity.<sup>25</sup> This sheds light on a more efficient steerable PAL calculation method.

This paper proposes a modified GBE method to calculate the sound field generated by a steerable PAL, which is termed a steerable non-paraxial GBE. To do this, two modifications are applied to the conventional GBE approach. First, the ultrasound and the audio sound are calculated in a rotated coordinate system, which is aligned to the steering direction so that the Rayleigh integral can be simplified and the mainlobe of the ultrasound can be included in the computation. Second, a non-paraxial approximation is adopted to simplify the volume integral to a onefold integral and two uncoupled summations. Numerical results for cases without beam steering, as well as with one-beam and dual-beam steering, are presented here. The efficacy of the proposed method is demonstrated by comparison with predictions obtained using a conventional GBE approach and an exact solution.

## II. QUASILINEAR SOLUTION AND CONVENTIONAL GAUSSIAN BEAM EXPANSION

### A. Physical model

As shown in Fig. 1, a Cartesian coordinate system  $Oxyz$  is established with the origin  $O$  at the center of a rectangular steerable PAL. The side lengths of the PAL in the  $x$  and  $y$  direction are  $2a_x$  and  $2a_y$ , respectively. The  $z$  axis is perpendicular to the radiation surface of the PAL. The rectangular steerable PAL generates two harmonic ultrasound waves at frequencies  $f_1$  and  $f_2$  ( $f_1 > f_2$ ) and the boundary condition on the steerable PAL surface is

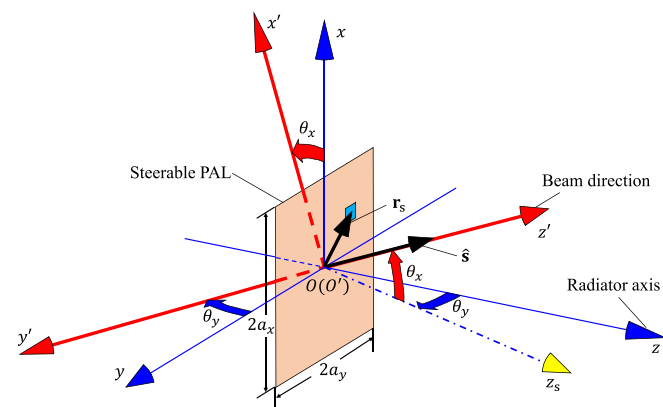


FIG. 1. (Color online) The sketch of a rectangular steerable PAL.

$$v_z(\mathbf{r}_s, t) = v_1(\mathbf{r}_s)e^{-i\omega_1 t} + v_2(\mathbf{r}_s)e^{-i\omega_2 t}, \quad (1)$$

where  $i$  is the imaginary unit,  $v_z$  represents the vibration velocity normal to the PAL surface,  $\mathbf{r}_s = (x_s, y_s, 0)$  is the surface source point,  $v_i(\mathbf{r}_s)$  is the complex amplitude of the vibration velocity at  $\mathbf{r}_s$ , and  $\omega_i = 2\pi f_i$  is the angular frequency of the ultrasound. Hereafter, the subscript  $i=1$  and  $2$  represents the index of the ultrasound at frequencies  $f_1$  and  $f_2$ , respectively.

The sound beam can be steered in an arbitrary direction based on the phased array technique. The beam direction can be described by a unit vector  $\hat{s} = (\sin \theta_x, \cos \theta_x \sin \theta_y, \cos \theta_x \cos \theta_y)$  with  $\theta_x$  the elevation angle and  $\theta_y$  the azimuth angle, as depicted in Fig. 1. The distribution of the vibration velocity on the surface of the steerable PAL can be expressed as

$$v_i(\mathbf{r}_s) = \begin{cases} v_0 \exp(i \operatorname{Re}[k_i] \mathbf{r}_s \cdot \hat{s}), & |x_s/a_x| < 1, |y_s/a_y| < 1 \\ 0, & \text{otherwise,} \end{cases} \quad (2)$$

where  $v_0$  is the amplitude of the vibration velocity,  $\operatorname{Re}[\cdot]$  indicates the real part,  $k_i = \omega_i/c_0 + i\alpha_i$  is the complex wavenumber of the ultrasound where  $\alpha_i$  is the sound attenuation coefficient due to atmospheric absorption,  $c_0$  is the sound speed in air, and the symbol “.” means the vector dot product. In Secs. II B, II C, and III, the audio sound field generated by a rectangular steerable PAL in this physical model will be calculated using different methods.

### B. Quasilinear solution

A quasilinear solution of the Westervelt equation is adopted first, as previous studies have demonstrated its validity when PALs are operated with the parameters used in this current work.<sup>7,14,15,17</sup> The audio sound pressure radiated by a PAL can be considered as a superposition of the pressure radiated by infinite virtual audio sources in air with the source density proportional to the ultrasound sound pressure. The audio sound pressure can be calculated as<sup>17</sup>

$$p_a(\mathbf{r}) = -\frac{i\omega_a \rho_0}{4\pi} \iiint_V q(\mathbf{r}_v) \frac{\exp(i k_a d_v)}{d_v} d^3 \mathbf{r}_v, \quad (3)$$

where  $\omega_a$  is the angular frequency of the audio sound,  $\rho_0$  is the air density,  $k_a = \omega_a/c_0$  is the wavenumber of the audio sound, and  $d_v = |\mathbf{r} - \mathbf{r}_v|$  is the distance between the field point  $\mathbf{r}$  and the virtual audio source point  $\mathbf{r}_v$ . The integration domain  $V$  represents a three-dimensional space, and the source density at the virtual source point  $\mathbf{r}_v$  can be expressed as<sup>17</sup>

$$q(\mathbf{r}_v) = -\frac{i\beta\omega_a}{\rho_0^2 c_0^4} p_1(\mathbf{r}_v) p_2^*(\mathbf{r}_v), \quad (4)$$

where  $\beta$  is the nonlinearity coefficient, the superscript “\*” denotes the complex conjugate, and  $p_1$  and  $p_2$  are the ultrasound pressure with the frequency of  $f_1$  and  $f_2$  at the virtual source point  $\mathbf{r}_v$ . The ultrasound pressure can be computed using a Rayleigh integral as<sup>7</sup>

$$p_i(\mathbf{r}_v) = -\frac{i\omega_i \rho_0}{2\pi} \iint_S v_i(\mathbf{r}_s) \frac{\exp(i k_i d_s)}{d_s} d^2 \mathbf{r}_s, \quad (5)$$

where  $d_s = |\mathbf{r}_v - \mathbf{r}_s|$  is the distance between the virtual audio source point  $\mathbf{r}_v$  and the PAL source point  $\mathbf{r}_s$ . The integration domain  $S$  represents the  $Oxy$  plane.

### C. Conventional Gaussian beam expansion (GBE)

The conventional GBE method adopts the paraxial approximation for both the ultrasound and the audio sound to simplify the Rayleigh integral in Eq. (5). It is usually used to model a conventional PAL without the beam steering, but it can also be extended to solve the radiation from a steerable PAL by multiplying the decomposed Gaussian functions by the steerable profile  $\exp(i k_i \mathbf{r}_s)$ .<sup>7,19</sup> The velocity distribution on the PAL surface can be expanded as the superposition of  $N$  Gaussian functions as<sup>22</sup>

$$v_i(\mathbf{r}_s) = v_0 \sum_{m_i=1}^N \sum_{n_i=1}^N A_{m_i} A_{n_i} \exp(-B_{m_i} x_s^2/a_x^2 - B_{n_i} y_s^2/a_y^2), \quad (6)$$

where  $A$  and  $B$  are the Gaussian expansion coefficients. These coefficients affect the approximation accuracy of the velocity profile on the radiation surface.<sup>22,26,27</sup> The paraxial approximation is used to approximate  $d_s$  in Eq. (5) in terms of several approximate terms as

$$d_s \approx z_v + \frac{(x_v - x_s)^2 + (y_v - y_s)^2}{2z_v}, \quad (7)$$

which is valid when  $(x_v - x_s)^2 + (y_v - y_s)^2 \ll z_v^2$ . To simplify the derivation, several dimensionless variables are introduced as

$$\tilde{x}_v = \frac{x_v}{a_x}, \quad \tilde{y}_v = \frac{y_v}{a_y}, \quad \tilde{z}_{v,x,i} = \frac{z_v}{\mathcal{R}_{x,i}}, \quad \tilde{z}_{v,y,i} = \frac{z_v}{\mathcal{R}_{y,i}}, \quad (8)$$

where the Rayleigh distance  $\mathcal{R}_{x,i} = k_i a_x^2/2$ , and  $\mathcal{R}_{y,i} = k_i a_y^2/2$ . Equations (6)–(8) are substituted into Eq. (5)

to simplify the Rayleigh integral. Because the  $1/d_s$  term is a slowly varying function compared with the  $\exp(i k_i d_s)$  term in Eq. (5), the  $1/d_s$  term is replaced by  $1/z_v$  and  $d_s$  in the  $\exp(i k_i d_s)$  term is replaced by Eq. (7). Then, Eq. (5) can be simplified to give

$$\begin{aligned} p_i(\mathbf{r}_v) &= p_0 e^{ik_i z_v} \sum_{m_i=1}^N \frac{A_{m_i}}{\sqrt{i\pi \tilde{z}_{v,x,i}}} \\ &\times \int_{-\infty}^{\infty} \exp\left[i \frac{(\tilde{x}_v - \tilde{x}_s)^2}{\tilde{z}_{v,x,i}} - B_{m_i} \tilde{x}_s^2\right] d\tilde{x}_s \\ &\times \sum_{n_i=1}^N \frac{A_{n_i}}{\sqrt{i\pi \tilde{z}_{v,y,i}}} \\ &\times \int_{-\infty}^{\infty} \exp\left[i \frac{(\tilde{y}_v - \tilde{y}_s)^2}{\tilde{z}_{v,y,i}} - B_{n_i} \tilde{y}_s^2\right] d\tilde{y}_s, \end{aligned} \quad (9)$$

where  $p_0 = \rho_0 c_0 v_0$ . By using the integral given by Eq. (5) in Ref. 21

$$\begin{aligned} &\int_{-\infty}^{\infty} \exp\left[i \frac{(x - x_s)^2}{\gamma} - \eta x_s\right] dx_s \\ &= \frac{\sqrt{i\pi\gamma}}{\sqrt{1+i\gamma\eta}} \exp\left(-\frac{\eta}{1+i\gamma\eta} x^2\right), \quad \text{Re}[\eta] > 0, \gamma \neq 0, \end{aligned} \quad (10)$$

and with some straightforward derivation, the ultrasound pressure at  $\mathbf{r}_v$  can be expressed as

$$\begin{aligned} p_i(\mathbf{r}_v) &= p_0 e^{ik_i z_v} \sum_{m_i=1}^N A_{m_i} G(\tilde{x}_v, \tilde{z}_{v,x,i}, B_{m_i}) \\ &\times \sum_{n_i=1}^N A_{n_i} G(\tilde{y}_v, \tilde{z}_{v,y,i}, B_{n_i}), \end{aligned} \quad (11)$$

where the Gaussian beam function is defined as

$$G(\xi, \zeta, B) = \frac{1}{\sqrt{1+iB\xi}} \exp\left(-\frac{B}{1+iB\xi} \xi^2\right). \quad (12)$$

The conventional GBE method simplifies the twofold integral given by Eq. (5) to two uncoupled summations. However, the accuracy of the conventional GBE method is poor when the steering angle is large (over 20°) or the field point is outside of the paraxial approximation region.

By applying the paraxial approximation in Eq. (7), the distance between the field point and the virtual source point  $d_v$  in Eq. (3) can be approximated as

$$d_v \approx |z - z_v| + \frac{(x - x_v)^2 + (y - y_v)^2}{2|z - z_v|}. \quad (13)$$

After substituting Eq. (11) into Eq. (4), the source density function can be expressed as

$$q(\mathbf{r}_v) = \frac{\beta k_a p_0^2}{i\rho_0^2 c_0^3} e^{i(k_1 - k_2^*) z_v} \sum_{m_1, m_2, n_1, n_2=1}^N A_{x, m_1, m_2} A_{y, n_1, n_2} \\ \times \exp(-B_{x, m_1, m_2} \tilde{x}_v^2 - B_{y, n_1, n_2} \tilde{y}_v^2), \quad (14)$$

where the new coefficients  $A$  and  $B$  can be expressed as

$$A_{\eta, m_1, m_2} = \frac{A_{m_1}}{\sqrt{1 + iB_{m_1} \tilde{z}_{v, \eta, 1}}} \left( \frac{A_{m_2}}{\sqrt{1 + iB_{m_2} \tilde{z}_{v, \eta, 2}}} \right)^*, \\ B_{\eta, m_1, m_2} = \frac{B_{m_1}}{1 + iB_{m_1} \tilde{z}_{v, \eta, 1}} + \left( \frac{B_{m_2}}{1 + iB_{m_2} \tilde{z}_{v, \eta, 2}} \right)^*, \quad (\eta = x, y). \quad (15)$$

It can be seen that the source density function [Eq. (14)] has the same form as the vibration velocity function [Eq. (6)]; therefore, the volume integral can be simplified in a form similar to the Rayleigh integral. After substituting Eqs. (13) and (14) into Eq. (3), the audio sound is written as

$$p_a(\mathbf{r}) = \frac{\beta k_a p_0^2}{2i\rho_0 c_0^2} \int_0^\infty e^{i[k_a(|z-z_v|) + (k_1 - k_2^*) z_v]} \\ \times \sum_{m_1, m_2=1}^N \frac{A_{x, m_1, m_2}}{\sqrt{i\pi \tilde{z}_{a,x}}} \\ \times \int_{-\infty}^\infty \exp \left[ i \frac{(\tilde{x} - \tilde{x}_v)^2}{\tilde{z}_{a,x}} - B_{x, m_1, m_2} \tilde{x}_v^2 \right] d\tilde{x}_v \\ \times \sum_{n_1, n_2=1}^N \frac{A_{y, n_1, n_2}}{\sqrt{i\pi \tilde{z}_{a,y}}} \\ \times \int_{-\infty}^\infty \exp \left[ i \frac{(\tilde{y} - \tilde{y}_v)^2}{\tilde{z}_{a,y}} - B_{y, n_1, n_2} \tilde{y}_v^2 \right] d\tilde{y}_v dz_v, \quad (16)$$

where dimensionless variables are introduced as

$$\tilde{z}_{a,x} = \frac{|z - z_v|}{\mathcal{R}_{a,x}}, \quad \tilde{z}_{a,y} = \frac{|z - z_v|}{\mathcal{R}_{a,y}}, \quad (17)$$

with the Rayleigh distance  $\mathcal{R}_{a,x} = k_a a_x^2 / 2$  and  $\mathcal{R}_{a,y} = k_a a_y^2 / 2$ . By using the integral given by Eq. (10), the integral in Eq. (16) can be simplified to

$$p_a(\mathbf{r}) = \frac{\beta p_0^2}{2i\rho_0 c_0^2} \int_0^\infty e^{i[k_a(|z-z_v|) + (k_1 - k_2^*) z_v]} \\ \times \sum_{m_1, m_2=1}^N A_{x, m_1, m_2} G(\tilde{x}, \tilde{z}_{a,x}, B_{x, m_1, m_2}) \\ \times \sum_{n_1, n_2=1}^N A_{y, n_1, n_2} G(\tilde{y}, \tilde{z}_{a,y}, B_{y, n_1, n_2}) k_a dz_v, \quad (18)$$

which is the expression typically obtained when using the conventional GBE method.

### III. STEERABLE NON-PARAXIAL GAUSSIAN BEAM EXPANSION

#### A. Rotated coordinates

As shown in Fig. 1, a rotated coordinate system  $O'x'y'z'$  is established with the origin  $O'$  at the center of the PAL. The positive  $z'$ -axis coincides with the beam direction  $\hat{s}$ . The rotated coordinates can be obtained by rotating the original coordinates twice. The first step is to rotate the original coordinate system around the  $x$  axis by an angle of  $\theta_y \in (-\pi/2, \pi/2)$ , and the  $y'$ -axis is then determined as shown in Fig. 1. The second step is to rotate the coordinate system around the  $y'$ -axis by an angle of  $\theta_x \in (-\pi/2, \pi/2)$ . The positive value of  $\theta_x$  (or  $\theta_y$ ) represents a rotation from the positive  $z_s$  (or  $z$ ) axis to the positive  $x$  (or  $y$ ) axis, whereas the negative value corresponds to a rotation towards the minus  $x$  (or  $y$ ) axis. The coordinate of a field point  $\mathbf{r}$  can be transformed to  $\mathbf{r}'$  by using a rotation matrix  $\mathbf{R}$  as

$$\mathbf{r}' = \mathbf{R}\mathbf{r}. \quad (19)$$

The rotation matrix  $\mathbf{R}$  can be obtained by using two basic rotation matrices,

$$\mathbf{R} = \mathbf{R}_y(-\theta_x)\mathbf{R}_x(\theta_y) \\ = \begin{bmatrix} \cos \theta_x & -\sin \theta_x \sin \theta_y & -\sin \theta_x \cos \theta_y \\ 0 & \cos \theta_y & -\sin \theta_y \\ \sin \theta_x & \cos \theta_x \sin \theta_y & \cos \theta_x \cos \theta_y \end{bmatrix}, \quad (20)$$

where

$$\mathbf{R}_x(\theta_y) = \begin{bmatrix} 1 & 0 & 0 \\ 0 & \cos \theta_y & -\sin \theta_y \\ 0 & \sin \theta_y & \cos \theta_y \end{bmatrix}, \\ \mathbf{R}_y(-\theta_x) = \begin{bmatrix} \cos \theta_x & 0 & -\sin \theta_x \\ 0 & 1 & 0 \\ \sin \theta_x & 0 & \cos \theta_x \end{bmatrix}. \quad (21)$$

Because  $\mathbf{R}$  is an orthogonal matrix,  $\mathbf{R}^{-1} = \mathbf{R}^T$ , where  $\mathbf{R}^{-1}$  is the inverse matrix of  $\mathbf{R}$ , and the superscript “T” denotes the transpose. The inverse transformation from  $\mathbf{r}'$  to  $\mathbf{r}$  can be expressed as

$$\mathbf{r} = \mathbf{R}^{-1}\mathbf{r}' = \mathbf{R}^T\mathbf{r}'. \quad (22)$$

Under the primed coordinates, the beam direction is denoted by the vector  $\hat{s}' = (0, 0, 1)$ . By using the inverse transformation in Eq. (22), the beam direction under the original coordinates can be obtained as  $\hat{s} = (\sin \theta_x, \cos \theta_x \sin \theta_y, \cos \theta_x \cos \theta_y)$ .

#### B. Ultrasound field

The velocity distribution given by Eq. (2) can be expanded using a summation of  $N$  Gaussian functions

$$v_i(\mathbf{r}_s) = v_0 \exp(i k_i \mathbf{r}_s \cdot \hat{\mathbf{s}}) \sum_{m_i=1}^N \sum_{n_i=1}^N A_{m_i} A_{n_i} \exp(-B_{m_i} x_s^2/a_x^2 - B_{n_i} y_s^2/a_y^2). \quad (23)$$

The  $d_s$  in Eq. (5) can be transformed to  $d'_s$  under the rotated coordinates

$$d'_s = |\mathbf{r}'_v - \mathbf{r}'_s| = |\mathbf{r}'_v - \mathbf{R}\mathbf{r}_s| = \sqrt{(x'_v - x_s \cos \theta_x + y_s \sin \theta_x \sin \theta_y)^2 + (y'_v - y_s \cos \theta_y)^2 + (z'_v - z'_s)^2}. \quad (24)$$

The ultrasound beam can be treated as a collimated beam, so  $d'_s$  can be approximated by using the paraxial approximation. After neglecting  $y_s \sin \theta_x \sin \theta_y$ , we obtain the approximation as

$$d'_s \approx |z'_v - z'_s| + \frac{(x'_v - x_s \cos \theta_x)^2 + (y'_v - y_s \cos \theta_y)^2}{2|z'_v - z'_s|}. \quad (25)$$

Similar to Eqs. (8) and (17), the following dimensionless variables are introduced in the rotated coordinates

$$\begin{aligned} \tilde{x}'_v &= \frac{x'_v}{a_x \cos \theta_x}, & \tilde{y}'_v &= \frac{y'_v}{a_y \cos \theta_y}, & \tilde{z}'_{v,x,i} &= \frac{z'_v}{\mathcal{R}'_{x,i}}, \\ \tilde{z}'_{v,y,i} &= \frac{z'_v}{\mathcal{R}'_{y,i}}, & \tilde{x}_s &= \frac{x_s}{a_x \cos \theta_x}, & \tilde{y}_s &= \frac{y_s}{a_y \cos \theta_y}, \end{aligned} \quad (26)$$

where the Rayleigh distance  $\mathcal{R}'_{x,i} = k_i a_x^2 \cos^2 \theta_x / 2$ ,  $\mathcal{R}'_{y,i} = k_i a_y^2 \cos^2 \theta_y / 2$ . The key contribution here is to project the sides  $a_x$  and  $a_y$  onto the primed  $x$  and  $y$  axes, respectively. When the rotation angles  $\theta_x = \theta_y = 0$ , these substitutions reduce to those given by Eqs. (8) and (17). Because of the sharp directivity of the ultrasound, the ultrasound in the region  $z < z'_s$  can be ignored,  $|z'_v - z'_s|$  can then be approximated by  $z'_v - z'_s$  and can be approximated by  $z'_v$  when it is the denominator in Eq. (25). By substituting Eq. (23) and Eq. (25) into Eq. (5), the Rayleigh integral for calculating the ultrasound can be written as

$$\begin{aligned} p_i(\mathbf{r}'_v) &= p_0 e^{ik_i z'_v} \sum_{m_i=1}^N \frac{A_{m_i}}{\sqrt{i \pi \tilde{z}'_{v,x,i}}} \\ &\times \int_{-\infty}^{\infty} \exp \left[ i \frac{(\tilde{x}'_v - \tilde{x}_s)^2}{\tilde{z}'_{v,x,i}} - B_{m_i} \cos^2 \theta_x \tilde{x}_s^2 \right] d\tilde{x}_s \\ &\times \sum_{n_i=1}^N \frac{A_{n_i}}{\sqrt{i \pi \tilde{z}'_{v,y,i}}} \int_{-\infty}^{\infty} \exp \left[ i \frac{(\tilde{y}'_v - \tilde{y}_s)^2}{\tilde{z}'_{v,y,i}} \right. \\ &\quad \left. - B_{n_i} \cos^2 \theta_y \tilde{y}_s^2 \right] d\tilde{y}_s. \end{aligned} \quad (27)$$

By using the integral formula Eq. (10), Eq. (27) can be simplified to

$$\begin{aligned} p_i(\mathbf{r}'_v) &= p_0 e^{ik_i z'_v} \sum_{m_i=1}^N A_{m_i} G\left(\tilde{x}'_v, \tilde{z}'_{v,x,i}, B_{m_i} \cos^2 \theta_x\right) \\ &\times \sum_{n_i=1}^N A_{n_i} G\left(\tilde{y}'_v, \tilde{z}'_{v,y,i}, B_{n_i} \cos^2 \theta_y\right), \end{aligned} \quad (28)$$

which is the ultrasound pressure in rotated coordinates. This expression reduces to Eq. (11) when the steering angles  $\theta_x = \theta_y = 0$ . By using the primed coordinates, the primary energy of the ultrasound can be contained using the Rayleigh integral.

### C. Audio sound

Because the audio sound at low frequencies cannot be treated as a narrow beam, the paraxial approximation given by Eq. (13) contains significant inaccuracies as demonstrated in Ref. 7. Instead, a non-paraxial approximation is used here to approximate  $d_v$  in Eq. (3) under rotated coordinates

$$d'_v = |\mathbf{r}' - \mathbf{r}'_v| \approx R'_v + \frac{(x' - x'_v)^2 + (y' - y'_v)^2}{2R'_v} - \frac{x'^2 + y'^2}{2R'_v}, \quad (29)$$

where  $R'_v = \sqrt{x'^2 + y'^2 + (z' - z'_v)^2}$ . The advantage of using a non-paraxial approximation over the paraxial approximation is illustrated in Fig. 2. The paraxial approximation uses  $|z - z_v|$  as the first-order approximation term of  $|\mathbf{r} - \mathbf{r}_v|$ , while  $R_v$  is adopted in the non-paraxial approximation. Because of the sharp directivity of the ultrasound, the source density of the virtual audio source is large near the  $z$  axis. Taking a virtual source point close to the  $z$  axis as an example, when the field point  $\mathbf{r}$  is located away from the  $z$  axis as  $|x|$  increases, the error of using  $|z - z_v|$  to approximate  $|\mathbf{r} - \mathbf{r}_v|$  is apparently much larger than using  $R_v$ .

By substituting the ultrasound pressure from Eq. (28) into Eq. (4), the virtual audio source density in the rotated coordinates can be expressed as

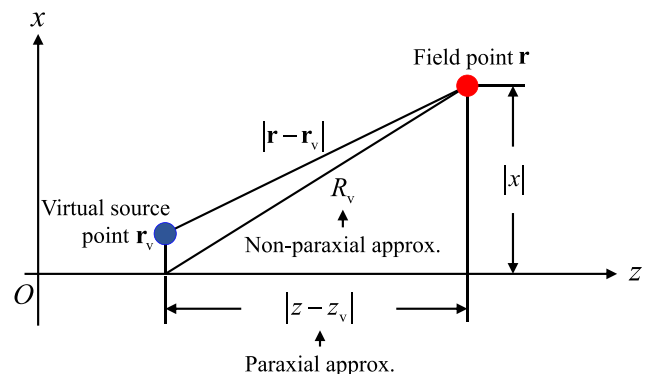


FIG. 2. (Color online) The sketch of the difference between paraxial and non-paraxial approximations.

$$q(\mathbf{r}') = \frac{\beta k_a p_0^2}{i\rho_0^2 c_0^2} e^{i(k_1 - k_2^*) z'_v} \sum_{m_1, m_2, n_1, n_2=1}^N A'_{x, m_1, m_2} A'_{y, n_1, n_2} \\ \times \exp\left(-B'_{x, m_1, m_2} \tilde{x}'_v^2 - B'_{y, n_1, n_2} \tilde{y}'_v^2\right), \quad (30)$$

where the primed coefficients  $A'$  and  $B'$  are defined as

$$A'_{\eta, m_1, m_2} = \frac{A_{m_1}}{\sqrt{1 + iB_{m_1} \cos^2 \theta_\eta \tilde{z}'_{v, \eta, 1}}} \\ \times \left( \frac{A_{m_2}}{\sqrt{1 + iB_{m_2} \cos^2 \theta_\eta \tilde{z}'_{v, \eta, 2}}} \right)^*, \quad (31)$$

$$B'_{\eta, m_1, m_2} = \frac{B_{m_1} \cos^2 \theta_\eta}{1 + iB_{m_1} \cos^2 \theta_\eta \tilde{z}'_{v, \eta, 1}} \\ + \left( \frac{B_{m_2} \cos^2 \theta_\eta}{1 + iB_{m_2} \cos^2 \theta_\eta \tilde{z}'_{v, \eta, 2}} \right)^*, \quad (\eta = x, y).$$

The dimensionless variables are introduced as

$$\tilde{R}'_x = \frac{R'_v}{\mathcal{R}'_{x,a}}, \quad \tilde{R}'_y = \frac{R'_v}{\mathcal{R}'_{y,a}}, \quad (32)$$

where the Rayleigh distance  $\mathcal{R}'_{x,a} = k_a a_x^2 \cos^2 \theta_x / 2$ ,  $\mathcal{R}'_{y,a} = k_a a_y^2 \cos^2 \theta_y / 2$ . By substituting Eqs. (29) and (30) into Eq. (3), the audio sound in the rotated coordinates can be expressed as

$$p_a(\mathbf{r}') = \frac{\beta k_a p_0^2}{2i\rho_0^2 c_0^2} \int_0^\infty e^{i[k_a R'_v + (k_1 - k_2^*) z'_v]} e^{-ik_a(x'^2 + y'^2)/R'_v} \\ \times \sum_{m_1, m_2=1}^N \frac{A'_{x, m_1, m_2}}{\sqrt{i\pi \tilde{R}'_x}} \\ \times \int_{-\infty}^\infty \exp\left[i \frac{(\tilde{x}' - \tilde{x}'_v)^2}{\tilde{R}'_x} - B'_{x, m_1, m_2} \tilde{x}'_v^2\right] d\tilde{x}'_v \\ \times \sum_{n_1, n_2=1}^N \frac{A'_{y, n_1, n_2}}{\sqrt{i\pi \tilde{R}'_y}} \\ \times \int_{-\infty}^\infty \exp\left[i \frac{(\tilde{y}' - \tilde{y}'_v)^2}{\tilde{R}'_y} - B'_{y, n_1, n_2} \tilde{y}'_v^2\right] d\tilde{y}'_v dz'_v. \quad (33)$$

By using the integral formula Eq. (10), the integral expression Eq. (33) can be simplified to

$$p_a(\mathbf{r}') = \frac{\beta k_a p_0^2}{2i\rho_0^2 c_0^2} \int_0^\infty e^{i[k_a R'_v + (k_1 - k_2^*) z'_v]} e^{-ik_a(x'^2 + y'^2)/R'_v} \\ \times \sum_{m_1, m_2=1}^N A'_{x, m_1, m_2} G\left(\tilde{x}', \tilde{R}', B'_{x, m_1, m_2}\right) \\ \times \sum_{n_1, n_2=1}^N A'_{y, n_1, n_2} G\left(\tilde{y}', \tilde{R}', B'_{y, n_1, n_2}\right) dz'_v, \quad (34)$$

which is the main result for the proposed steerable non-paraxial GBE. The audio sound in the original coordinate can be obtained by substituting inverse transformation Eq. (22) into Eq. (34).

The calculation process for the steerable non-paraxial GBE method can be described in two steps. First, the field point  $\mathbf{r}$  is transformed to  $\mathbf{r}'$  by using the rotation transformation given by Eq. (19). Then, the audio sound in rotated coordinates system can be calculated using Eq. (34). In Eq. (34), the coefficients  $A'$  and  $B'$  can be obtained by Eq. (31), and the Gaussian beam function is calculated using Eq. (12). The dimensionless variables involved in the calculations are obtained using Eqs. (26) and (32).

When the steering angles  $\theta_x = \theta_y = 0$  and the field point are located close to the radiator axis,  $R'_v \approx |z' - z'_v|$ , Eq. (34) reduces to Eq. (18). Therefore, the proposed steerable non-paraxial GBE is seen as an extension of the conventional GBE. The improvement of the proposed method lies in two aspects. As illustrated in Fig. 1, the first aspect is rotating the coordinate system so that the mainlobe of the ultrasound beam is aligned to one axis. This ensures that the major part of ultrasound energy is included in the paraxial region in the rotated coordinates. The allowed steering angle is limited by the approximation made in Eq. (24), i.e., neglecting  $y_s \sin \theta_x \sin \theta_y$ . This term is zero if no steering is made in the  $x$  direction ( $\theta_x = 0$ ), indicating that the allowed steering angle in the  $y$  direction can be as large as up to 90°. The second aspect is the introduction of the non-paraxial approximation for audio sound as demonstrated in Fig. 2. This allows for more accurate predictions of audio sound at wide observation angles. The numerical results in Sec. IV show that predictions with an acceptable accuracy are within ±30° with respect to the beam direction. Although the proposed method is more accurate than the conventional GBE, they have the same computational cost as both methods only need to compute a onefold integral and the product of uncoupled summations of the Gaussian functions. This is much more efficient than computing the fivefold integral in Eq. (3). It is concluded that the proposed steerable non-paraxial GBE method outperforms the conventional one for predicting the audio sound field generated by a steerable PAL.

## D. Steerable PALs generating multiple beams

Steerable PALs generating multiple beams have been used to simultaneously form personal audio zones<sup>28</sup> and create virtual sound sources in a mixed reality system,<sup>29</sup> so the modeling of the audio sound generated by them is also of interest. When the sound beam is steered away from the radiator axis, the conventional GBE method is inaccurate because the mainlobe of the ultrasound lies away from the paraxial region.<sup>7</sup> Other existing methods, including the convolution directivity model,<sup>30</sup> cylindrical<sup>31</sup> and spherical<sup>32</sup> wave expansions, have different limitations. Here, we aim to show the calculation process for a steerable PAL

generating multiple beams based on the proposed steerable non-paraxial GBE.

The boundary condition on the steerable PAL generating multiple beams with different beam direction  $\hat{s}_j$  ( $j \in 1, 2, \dots, J$ ) can be expressed as

$$v_z(\mathbf{r}_s) = \sum_{j=1}^J v_{z,j}(\mathbf{r}_s), \quad (35)$$

where  $J$  is the number of directional beams and  $v_{z,j}(\mathbf{r}_s)$  is the velocity profile for generating the  $j$ -th beam in the direction  $\hat{s}_j$  which can be obtained by substituting  $\hat{s}_j$  in Eqs. (1) and (2). Then, the audio sound pressure is approximated by

$$p_a(\mathbf{r}) = \sum_{j=1}^J p_{a,j}(\mathbf{r}), \quad (36)$$

where  $p_{a,j}(\mathbf{r})$  is the audio sound pressure generated due to  $v_{z,j}(\mathbf{r}_s)$  and it can be calculated by the steerable non-paraxial GBE method. Note that Eq. (36) ignores the nonlinear interactions between the beams in different directions. This is generally acceptable for two reasons. First, the included angle between the directions of any two beams is usually more than  $20^\circ$ , resulting in a small overlap region where the nonlinear interactions happen. Second, the accumulative effects of these nonlinear interactions as characterized by Westervelt equation decay rapidly as the included angle between beams increases.

#### IV. NUMERICAL RESULTS

The parameters used in the simulations that follow are listed in Table I, where the center frequency of the ultrasound  $f_u = (f_1 + f_2)/2$ . Hereafter, the direct numerical computation of the quasilinear solution given by Eq. (3) is denoted as an “exact solution.” The integration domain of Eq. (3) is set as  $-0.4 \text{ m} \leq x'_v \leq 0.4 \text{ m}$ ,  $-0.4 \text{ m} \leq y'_v \leq 0.4 \text{ m}$ ,  $0 \leq z'_v \leq 4 \text{ m}$  to cover the major part of the ultrasonic beam.

The numerical results of the conventional GBE method and the steerable non-paraxial GBE method given by Eqs. (18) and (34) are denoted as “conventional GBE” and “steerable non-paraxial GBE,” respectively, and the integration domain in Eqs. (18) and (34) are set to be the same as  $0 \leq z'_v \leq 4 \text{ m}$ , which covers the major part of the ultrasonic

TABLE I. Parameters used in the simulations.

Parameters	Value
Ambient temperature	$T = 20^\circ\text{C}$
Relative humidity of air	$h_r = 60\%$
Size of the PAL	$a_x = 0.04 \text{ m}$ , $a_y = 0.02 \text{ m}$
Center frequency of the ultrasound	$f_u = 40 \text{ kHz}$
Attenuation coefficients of the ultrasound	$\alpha_u = 0.15 \text{ Np/m}$
Amplitude of the velocity profile	$v_0 = 0.14 \text{ m/s}$
Nonlinearity coefficient	$\beta = 1.2$

TABLE II. Computational cost of the conventional GBE, the steerable non-paraxial GBE, and the exact solution.

	Calculation time (s)	Required memory (GB)
Conventional GBE	0.07	0.004
Steerable non-paraxial GBE	0.09	0.004
Exact solution	1090.26	181.05

beam. Further simulations (not shown in this paper) show the error of this truncation to be less than 0.1 dB for the calculated audio sound. The Gaussian expansion coefficients are adopted from Table II in Ref. 27.

#### A. Conventional PAL without the beam steering

The conventional PAL without beam steering is examined first, so that  $\theta_x = \theta_y = 0$ . The axial audio sound generated by a conventional PAL at 500 Hz and 4 kHz along the positive  $z'$  axis using each method is shown in Fig. 3. Figure 3 also shows the audio sound pressure level (SPL) error defined as the difference between the exact solution and the SPL using both GBE methods. The distance between the axial field point  $(0, 0, z)$  and the virtual source point  $(x_v, y_v, z_v)$  is  $d_v = \sqrt{(z - z_v)^2 + \rho_v^2}$ , where  $\rho_v = \sqrt{x_v^2 + y_v^2}$ . It is observed that the predictions of axial sound pressure are the same for both GBE methods. The reason is that the non-paraxial approximation [Eq. (29)] used in the steerable non-paraxial GBE is equivalent to the paraxial approximation given by Eq. (13), i.e.,  $\tilde{d}_v = |z - z_v| + \rho_v^2/(2|z - z_v|)$ , when the field point is located on the radiator axis and the steering angles are  $\theta_x = \theta_y = 0$ . It is also found that the axial audio SPL error is larger in the near field. For example, the audio SPL increases from 0.1 to 1 dB when the radial distance decreases from 1 to 0.2 m at 4 kHz. This can be attributed to the fact that the approximation given by Eq. (7) is not fully valid in the near field, which results in inaccurate calculations of the virtual sound source density in the near field.<sup>22</sup> It can also be observed that the axial audio SPL error in the near field is larger at lower audio frequencies. For example, the axial audio SPL error increases from 0.3 to 3 dB at 0.5 m away from the PAL when the audio frequency decreases from 4 kHz to 500 Hz. This behavior can be explained by looking into the error in the Green’s function used in calculating the radiation from the virtual audio sound source, which is  $\epsilon(\rho_v, k_a) = g(\tilde{d}_v, k_a) - g(d_v, k_a)$ , where  $g(d_v, k_a) = e^{ik_a d_v}/d_v$ . It is clear that the phase of the error oscillates with respect to the transverse distance of the virtual source point  $\rho_v$ , and the oscillation becomes smaller at low audio frequencies. In the limiting case with  $k_a \rightarrow 0$ , the error is approximately in-phase at different values of  $\rho_v$ ; therefore, the error becomes larger at lower audio frequencies.

Figure 4 shows the audio sound calculated by the three methods at different angles on the  $Oxz_s$  plane, 2 m from the conventional PAL to the field point. When the audio frequency is 4 kHz, it is observed that the predictions using

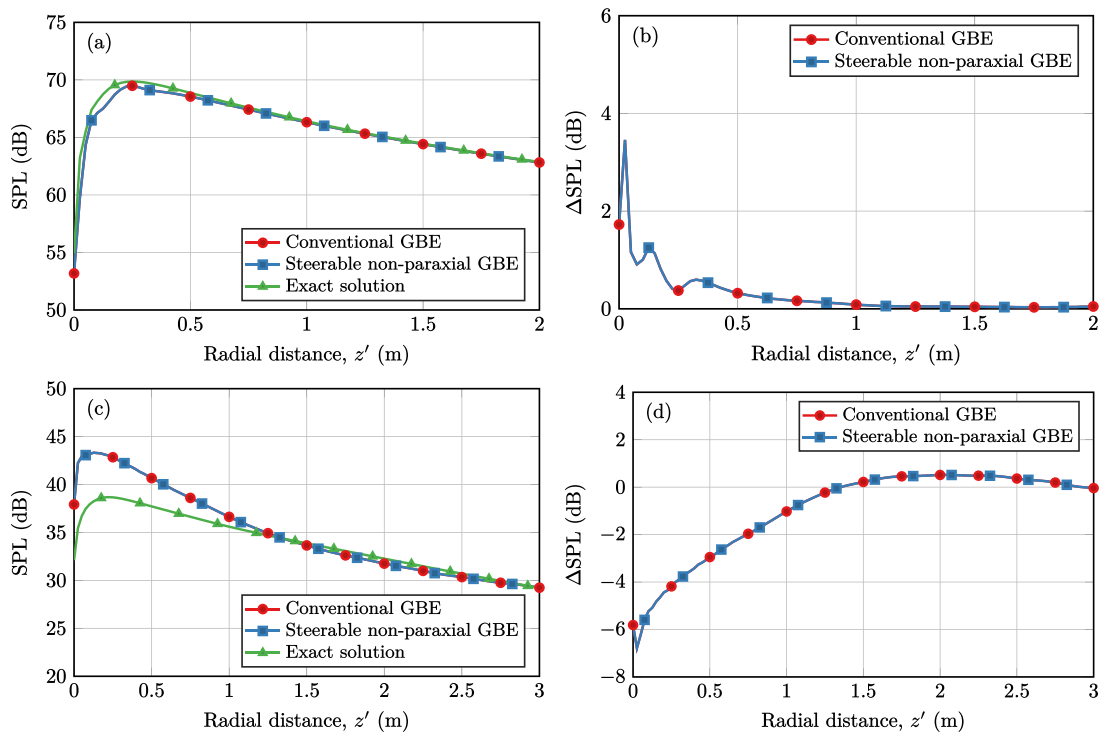


FIG. 3. (Color online) The axial audio sound pressure generated by a conventional PAL along the  $z'$  axis calculated by three methods. Top row, the audio frequency is 4 kHz; bottom row, the audio frequency is 500 Hz. Left column, axial SPL; right column, axial SPL error.

both GBE methods are similar when the angle is small because the non-paraxial approximation and the paraxial approximation have the same level of precision when the field point is near the  $z'$  axis. For example, the SPL error is

around 0.5 dB at  $5^\circ$  for both GBE methods. However, when the angle is  $40^\circ$ , the SPL error of the conventional GBE is around 10 dB, whereas the SPL error of the steerable non-paraxial GBE is only 0.1 dB. When the audio frequency is

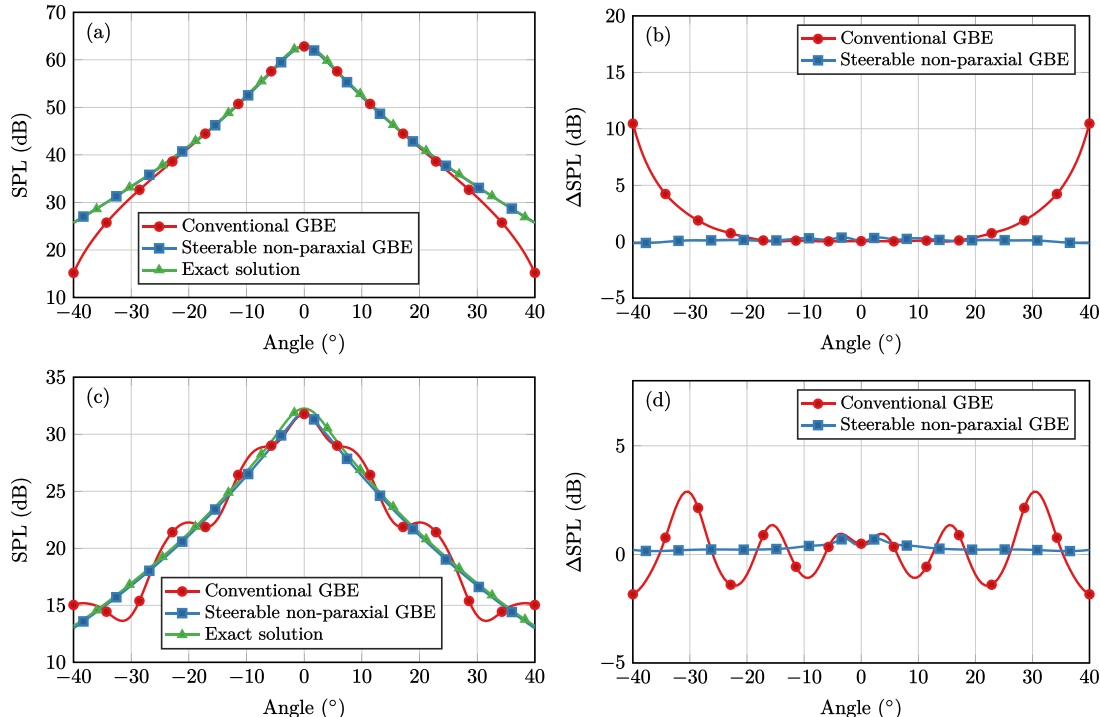


FIG. 4. (Color online) The angular audio sound field in the plane  $Oxz$  generated by a conventional PAL at a distance of 2 m. Top row, the audio frequency is 4 kHz; bottom row, the audio frequency is 500 Hz. Left column, angular audio SPL; right column, angular audio SPL error.

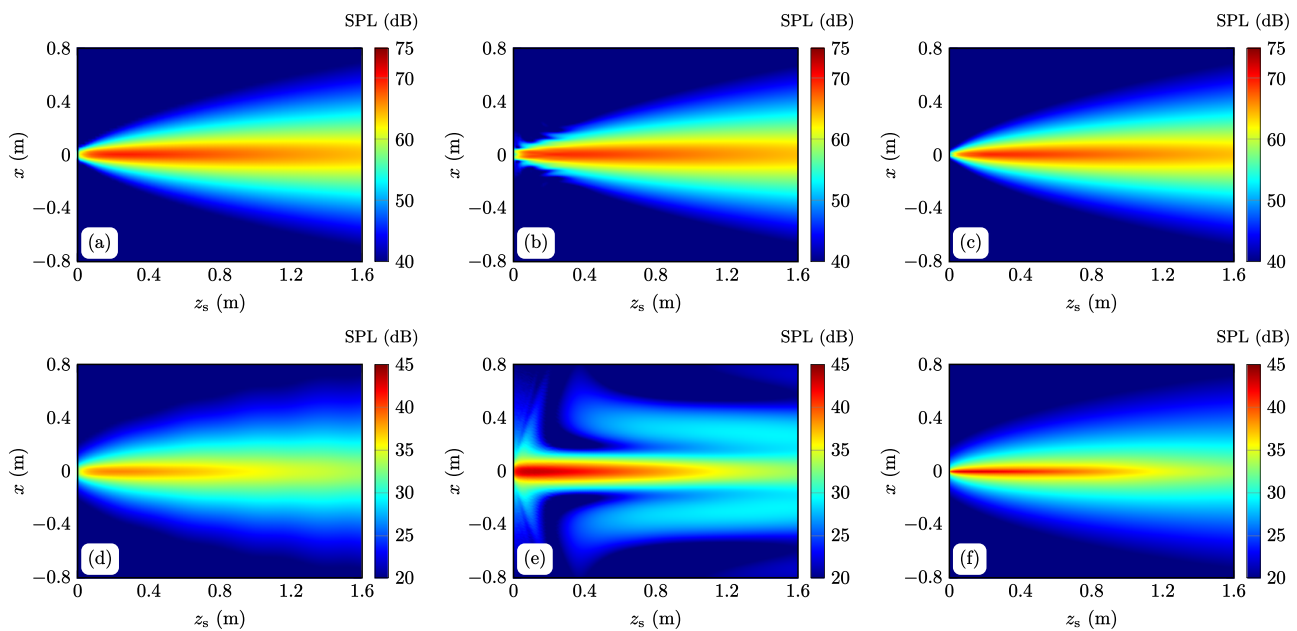


FIG. 5. (Color online) The 2D audio sound pressure field in the plane  $Oxz$  generated by the conventional PAL. Left column, exact solution; middle column, conventional GBE; right column, steerable non-paraxial GBE. Top row, the audio frequency is 4 kHz; bottom row, the audio frequency is 500 Hz.

500 Hz, the predictions using conventional GBE display large fluctuations while the prediction error for the steerable non-paraxial GBE is slightly increased. The maximum SPL error is 3 dB and 1 dB for the conventional and the steerable non-paraxial GBE, respectively, when the angle ranges from  $-40^\circ$  to  $40^\circ$ .

Figure 5 presents the two-dimensional (2D) distribution of the audio SPL calculated by different methods on the plane  $Oxz_s$ . It is observed that the conventional GBE method is accurate only within the paraxial region<sup>22</sup> ( $<20^\circ$ ), whereas the proposed modified GBE agrees much better with the exact solution. When the audio frequency is 500 Hz, it can be seen in Fig. 5(e) that the sound field calculated using the conventional GBE is also distorted, even in the paraxial region. The prediction accuracy is improved by using the proposed modified GBE [as shown in Fig. 5(f)], although the SPL is overestimated in the near field, which is discussed in the analysis of Fig. 3. The results presented in this subsection demonstrate that the steerable non-paraxial GBE outperforms the conventional GBE even for a conventional PAL without the beam steering.

## B. Steerable PAL generating one beam

A steerable PAL generating one beam with the steering angles  $\theta_x = -30^\circ$  and  $\theta_y = -35^\circ$  is considered in this subsection. The axial audio sound at different frequencies along the  $z'$  axis calculated by three methods is shown in Fig. 6. It can be seen that the prediction of the conventional GBE is much lower than the exact solution, whereas the steerable non-paraxial GBE maintains its accuracy at a level similar to that seen without beam steering in Fig. 3. For example, the maximal audio SPL error of the conventional GBE method is 17 dB at 4 kHz when the radial

distance ranges from 0 to 2 m, while it is only 2 dB for the steerable non-paraxial GBE. This is because the paraxial approximation used in conventional GBE is unable to contain the ultrasound beyond the paraxial region, whilst this is addressed in the proposed method by rotating the original coordinates so that the positive  $z'$  axis of the rotated (primed) coordinates is aligned with the beam's direction (see Fig. 1). Under the primed coordinate system, the paraxial approximation can be confidently adopted to include the mainlobe of the ultrasound waves. At a low audio frequency of 500 Hz, it is observed that the accuracy of the steerable non-paraxial GBE deteriorates in the near field. However, it is still superior to the conventional GBE.

Figure 7 presents the angular audio sound at different angles in the plane  $Oxz_s$ , 2 m from the steerable PAL using each method. It can be seen that the peak value for sound pressure predicted by the conventional GBE to lie at  $-22^\circ$  and  $-18^\circ$  at 4 kHz and 500 Hz, respectively, which deviates significantly from the steering angle of  $-30^\circ$ . This means that conventional GBE is not suitable for predicting the correct beam direction for a steerable PAL. However, by adopting the proposed steerable non-paraxial GBE, the correct beam direction is predicted exactly. Moreover, the proposed new method is more accurate over a wide range of steering angles. For example, the audio SPL error of the proposed method is less than 2 dB when the angle ranges from  $-50^\circ$  to  $-10^\circ$ , while the error using the conventional GBE can be larger than 30 dB.

Figure 8 shows the 2D audio sound field in the  $Oxz_s$  plane. It can be observed in Figs. 8(b) and 8(e) that the audio sound field obtained using conventional GBE distorts more significantly over the full sound field. However, in Figs. 8(c) and 8(f), it is seen that the steerable non-paraxial GBE maintains accuracy even at large beam steering angles.

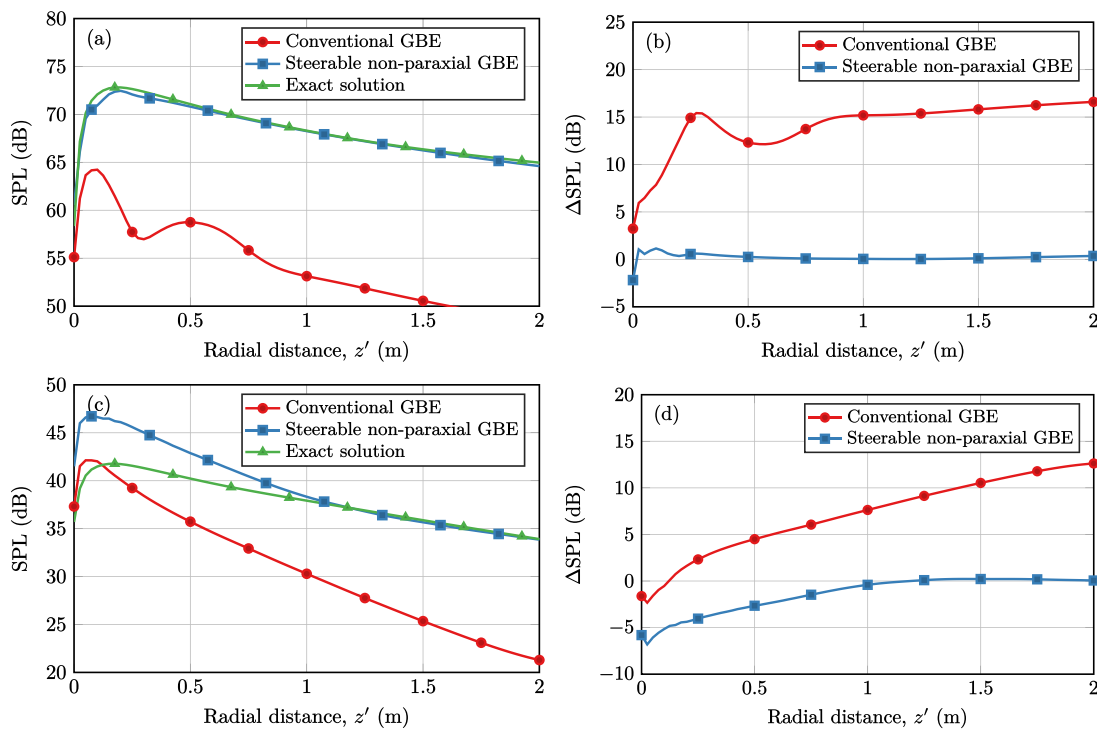


FIG. 6. (Color online) The axial audio sound pressure of the steering one beam generated by a steerable PAL along the  $z'$  axis calculated by three methods. Top row, the audio frequency is 4 kHz; bottom row, the audio frequency is 500 Hz. Left column, axial SPL; right column, axial SPL error.

### C. Steerable PAL generating dual beams

The generation of two beams with steering angles  $\theta_x = -35^\circ$ ,  $\theta_y = 0^\circ$ , and  $\theta_x = 35^\circ$ ,  $\theta_y = 0^\circ$ , is considered in this subsection. Figure 9 shows the angular audio sound at different angles in the plane  $Oxz_s$  with two steering beams,

2 m from the steerable PAL. The conventional GBE is again seen to predict wrong steering angles at  $\pm 28^\circ$  while they can be predicted exactly by the proposed steerable non-paraxial GBE method. Moreover, when the frequency decreases to 500 Hz, the audio sound calculated by the

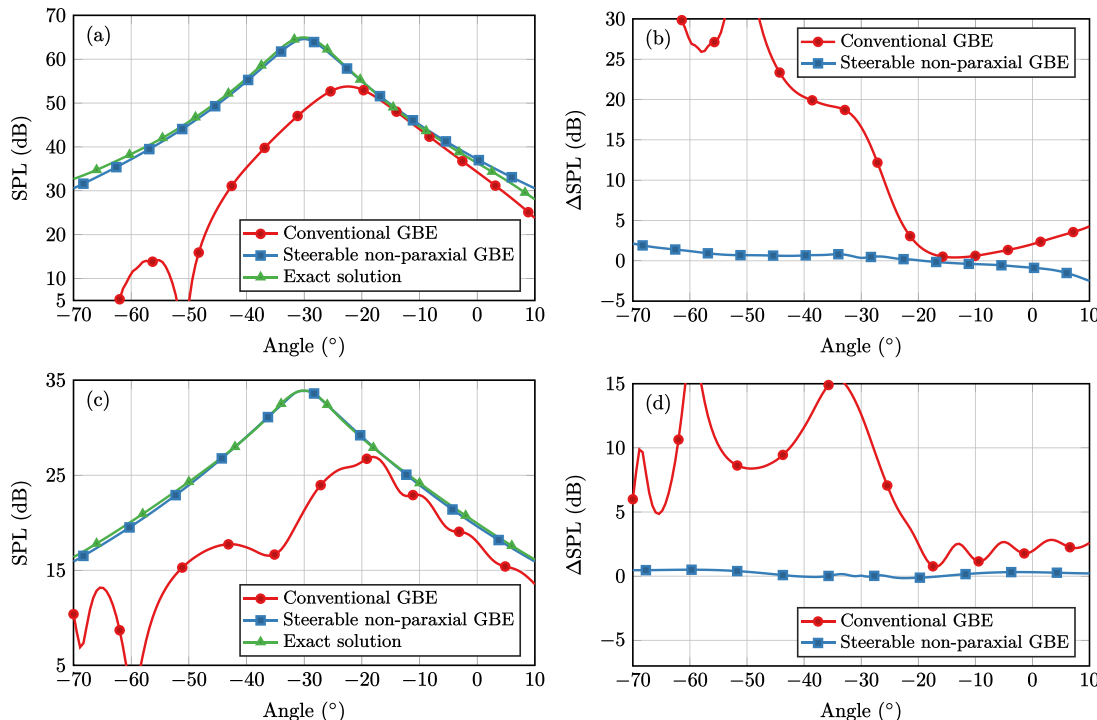


FIG. 7. (Color online) The angular audio sound field in the plane  $Oxz_s$  generated by a PAL steering one beam at  $-30^\circ$  at a distance of 2 m. Top row, the audio frequency is 4 kHz; bottom row, the audio frequency is 500 Hz. Left column, angular SPL; right column, angular SPL error.

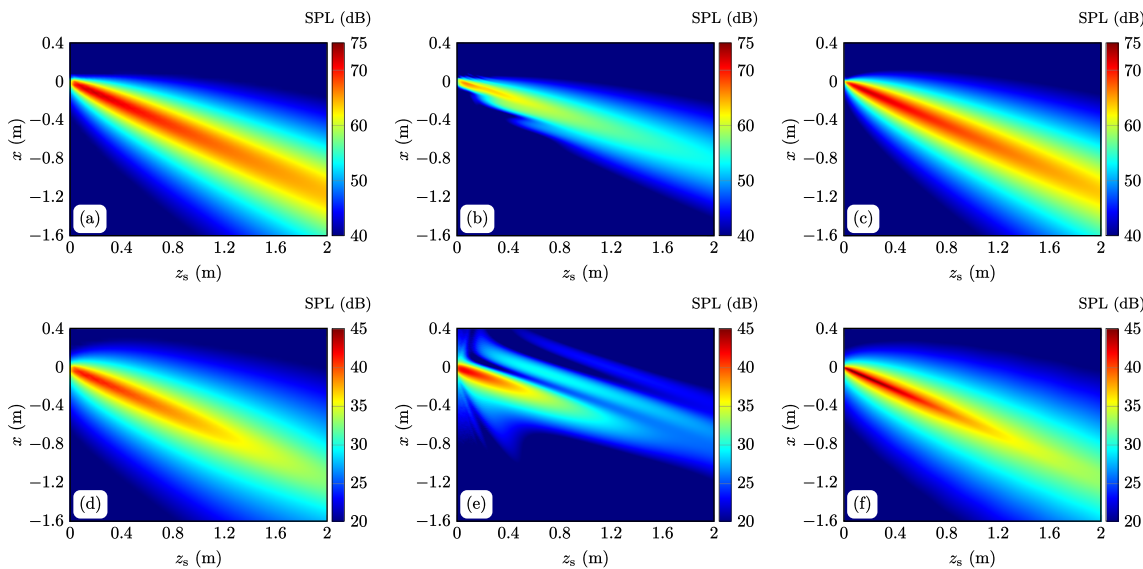


FIG. 8. (Color online) The 2D audio sound pressure field in the plane  $Oxz_s$  generated by the PAL steering one beam at  $-30^\circ$ . Left column, exact solution; middle column, conventional GBE; right column, steerable non-paraxial GBE. Top row, the audio frequency is 4kHz; bottom row, the audio frequency is 500Hz.

conventional GBE again shows significant fluctuations. The maximal SPL error using the conventional GBE is up to 18 dB for the angles ranging from  $-70^\circ$  to  $70^\circ$ , while it is only 1 dB for the steerable non-paraxial GBE.

Figure 10 shows the 2D audio sound field in the plane  $Oxz_s$  generated by a PAL steering two beams at  $\pm 35^\circ$ . It is clear that significant fluctuations are present when using the conventional GBE approach; however, the results using the steerable non-paraxial GBE are smooth when compared to

the exact solution and the prediction accuracy is much improved. All the above numerical results demonstrate the proposed steerable non-paraxial GBE method outperforms the conventional GBE for a PAL with and without beam steering. The improvement of the proposed method is more significant at large steering angles, low audio frequencies, and the points outside the paraxial region. It is also noted that both the conventional and steerable non-paraxial GBE methods are inaccurate in the near field. However, they are

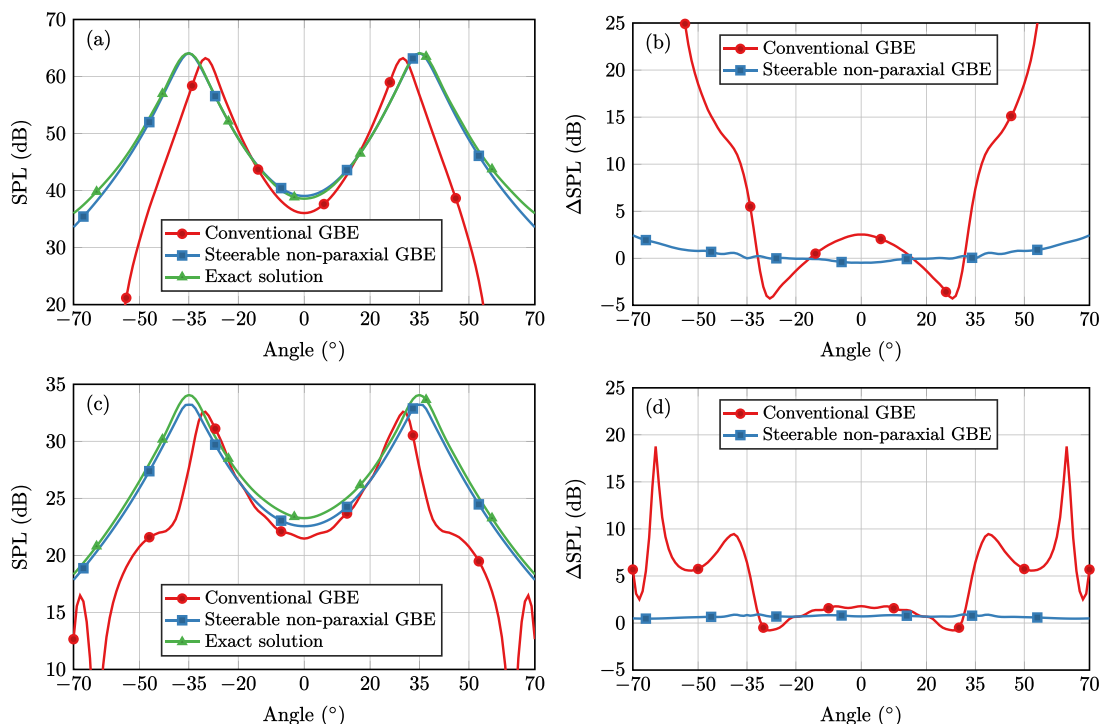


FIG. 9. (Color online) The angular audio sound field in the plane  $Oxz_s$  generated by a PAL steering two beams at  $\pm 35^\circ$  at a distance of 2 m. Top row, the audio frequency is 4 kHz; bottom row, the audio frequency is 500 Hz. Left column, angular SPL; right column, angular SPL error.

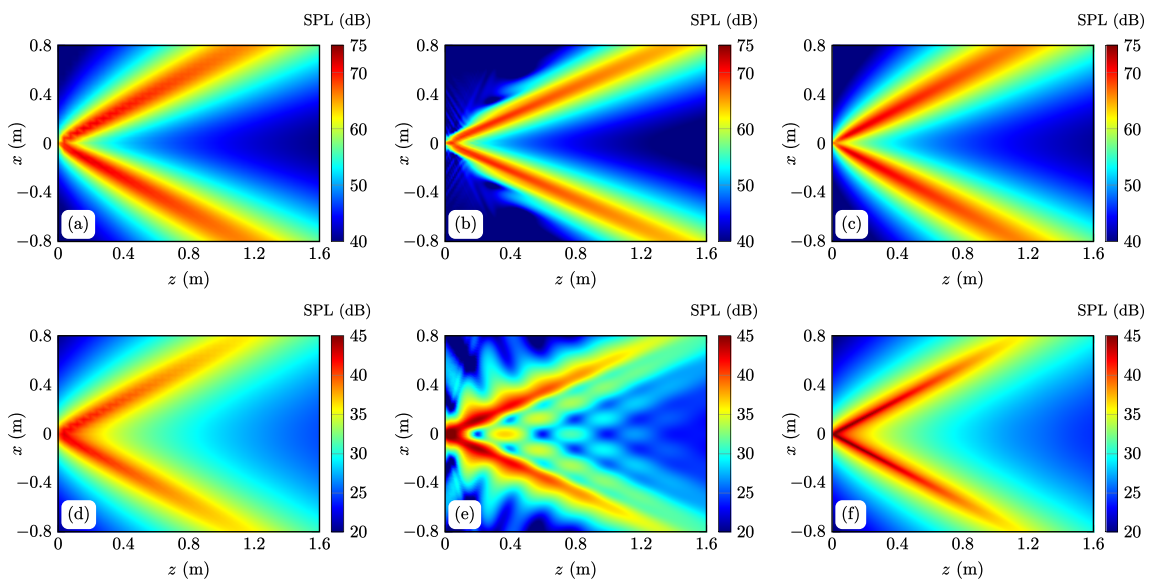


FIG. 10. (Color online) The 2D audio sound pressure field in the plane  $Oxz_s$  generated by the PAL steering two beams at  $\pm 35^\circ$ . Left column, exact solution; middle column, conventional GBE; right column, steerable non-paraxial GBE. Top row, the audio frequency is 4 kHz; bottom row, the audio frequency is 500 Hz.

based on the Westervelt equation which cannot correctly capture the local effects in the near field.<sup>14,15</sup> Therefore, they are not expected to be used to predict the sound field at the locations close to the PAL.

#### D. Computational cost of the proposed method

Table II shows the calculation time and the required memory of the conventional GBE, the steerable non-paraxial GBE, and the exact solution for an on-axis point ( $x = 0, y = 0, z = 1 \text{ m}$ ). The results are obtained on a computer with a 2.1 GHz central processing unit and 1 TB random access memory.

Although there is only one field point to be calculated, the computational time of the exact solution given by Eq. (3) is more than 1000 s, which is time-consuming because of the difficulty in the numerical evaluation of the fivefold integral. The required memory of the exact solution is very large because all the virtual points need to be stored. This is the reason why the direct integration of Eq. (3) has generally not been adopted in the literature. GBE-based methods can be more than 10 000 times faster and require much less memory because there is only a onefold integral and two uncoupled twofold summations to evaluate [see Eqs. (18) and (34)]. Due to this advantage, the GBE method is now widely used in the literature although it is shown here that this at the expense of inaccurate results in the near field. However, it is observed in Table II that the proposed steerable non-paraxial GBE method retains the advantages of computational efficiency as with the conventional GBE, but at the same time, it is capable of delivering significantly more accurate predictions for a steerable PAL.

#### V. CONCLUSION

An improved GBE method for calculating audio sound generated by a steerable PAL is proposed in this article. The

proposed method improves the conventional GBE approach in two ways: first, the coordinate system is rotated so that one of the axes coincides with the beam direction, this enables the mainlobe of the ultrasound waves to be computed when using a paraxial approximation; second, a non-paraxial approximation is used to improve the integration with respect to a virtual audio source, as this is more accurate than the paraxial approximation used in a conventional GBE approach. This means that the proposed method is capable of delivering more accurate off-axis predictions when compared to the conventional GBE method. The proposed method also retains the computational advantages of the conventional GBE method by reducing the fivefold integral of the quasilinear solution to a onefold integral and two uncoupled twofold summations. This means that the calculation time and the required memory of the proposed method are the same as the conventional GBE. Moreover, numerical results demonstrate that the proposed steerable non-paraxial GBE is more accurate than conventional GBE. Accordingly, it is concluded that the proposed steerable non-paraxial GBE outperforms the conventional GBE and provides a useful tool to analyze the audio sound field generated by a steerable PAL.

#### ACKNOWLEDGMENTS

T.Z. and J.L. gratefully acknowledge the financial support by the National Natural Science Foundation of China (Grant Nos. 11874219 and 12274221).

<sup>1</sup>P. J. Westervelt, “Parametric acoustic array,” *J. Acoust. Soc. Am.* **35**(4), 535–537 (1963).

<sup>2</sup>N. Tanaka and M. Tanaka, “Active noise control using a steerable parametric array loudspeaker,” *J. Acoust. Soc. Am.* **127**(6), 3526–3537 (2010).

<sup>3</sup>N. Tanaka and M. Tanaka, “Mathematically trivial control of sound using a parametric beam focusing source,” *J. Acoust. Soc. Am.* **129**(1), 165–172 (2011).

- <sup>4</sup>C. Shi, Y. Kajikawa, and W.-S. Gan, “An overview of directivity control methods of the parametric array loudspeaker,” *APSIPA Trans. Signal Inf. Process.* **3**, e20 (2014).
- <sup>5</sup>J. Zhong, T. Zhuang, R. Kirby, M. Karimi, H. Zou, and X. Qiu, “Quiet zone generation in an acoustic free field using multiple parametric array loudspeakers,” *J. Acoust. Soc. Am.* **151**(2), 1235–1245 (2022).
- <sup>6</sup>R. Iijima, S. Minami, Y. Zhou, T. Takehisa, T. Takahashi, Y. Oikawa, and T. Mori, “Audio hotspot attack: An attack on voice assistance systems using directional sound beams and its feasibility,” *IEEE Trans. Emerg. Top. Comput.* **9**(4), 2004–2018 (2019).
- <sup>7</sup>M. Červenka and M. Bednářík, “Non-paraxial model for a parametric acoustic array,” *J. Acoust. Soc. Am.* **134**(2), 933–938 (2013).
- <sup>8</sup>H. O. Berkay and D. J. Leahy, “Farfield performance of parametric transmitters,” *J. Acoust. Soc. Am.* **55**(3), 539–546 (1974).
- <sup>9</sup>C. Shi and W.-S. Gan, “Product directivity models for parametric loudspeakers,” *J. Acoust. Soc. Am.* **131**(3), 1938–1945 (2012).
- <sup>10</sup>C. Shi and Y. Kajikawa, “A convolution model for computing the far-field directivity of a parametric loudspeaker array,” *J. Acoust. Soc. Am.* **137**(2), 777–784 (2015).
- <sup>11</sup>O. Guasch and P. Sánchez-Martín, “Far-field directivity of parametric loudspeaker arrays set on curved surfaces,” *Appl. Math. Model.* **60**, 721–738 (2018).
- <sup>12</sup>C. Shi, Y. Wang, H. Xiao, and H. Li, “Extended convolution model for computing the far-field directivity of an amplitude-modulated parametric loudspeaker,” *J. Phys. D: Appl. Phys.* **55**(24), 244002 (2022).
- <sup>13</sup>S. I. Aanonsen, T. Barkve, J. N. Tjøtta, and S. Tjøtta, “Distortion and harmonic generation in the nearfield of a finite amplitude sound beam,” *J. Acoust. Soc. Am.* **75**(3), 749–768 (1984).
- <sup>14</sup>J. Zhong, R. Kirby, and X. Qiu, “The near field, Westervelt far field, and inverse-law far field of the audio sound generated by parametric array loudspeakers,” *J. Acoust. Soc. Am.* **149**(3), 1524–1535 (2021).
- <sup>15</sup>M. Červenka and M. Bednářík, “A versatile computational approach for the numerical modelling of parametric acoustic array,” *J. Acoust. Soc. Am.* **146**(4), 2163–2169 (2019).
- <sup>16</sup>W.-S. Gan, J. Yang, and T. Kamakura, “A review of parametric acoustic array in air,” *Appl. Acoust.* **73**(12), 1211–1219 (2012).
- <sup>17</sup>J. Zhong, R. Kirby, and X. Qiu, “A spherical expansion for audio sounds generated by a circular parametric array loudspeaker,” *J. Acoust. Soc. Am.* **147**(5), 3502–3510 (2020).
- <sup>18</sup>J. Wen and M. Breazeale, “A diffraction beam field expressed as the superposition of gaussian beams,” *J. Acoust. Soc. Am.* **83**(5), 1752–1756 (1988).
- <sup>19</sup>J. Yang, K. Sha, W.-S. Gan, and J. Tian, “Modeling of finite-amplitude sound beams: Second order fields generated by a parametric loudspeaker,” *IEEE Trans. Ultrason. Ferroelectr. Freq. Control* **52**(4), 610–618 (2005).
- <sup>20</sup>M. Ervenka and M. Bednářík, “On the structure of multi-gaussian beam expansion coefficients,” *Acta Acust. united Acust.* **101**(1), 15–23 (2015).
- <sup>21</sup>D. Ding, Y. Zhang, and J. Liu, “Some extensions of the Gaussian beam expansion: Radiation fields of the rectangular and the elliptical transducer,” *J. Acoust. Soc. Am.* **113**(6), 3043–3048 (2003).
- <sup>22</sup>H.-J. Kim, L. W. Schmerr, Jr., and A. Sedov, “Generation of the basis sets for multi-Gaussian ultrasonic beam models—An overview,” *J. Acoust. Soc. Am.* **119**(4), 1971–1978 (2006).
- <sup>23</sup>L. W. Schmerr, Jr., *Fundamentals of Ultrasonic Phased Arrays* (Springer, 2014), Vol. 215.
- <sup>24</sup>R. Huang, L. W. Schmerr, and A. Sedov, “Modeling the radiation of ultrasonic phased-array transducers with Gaussian beams,” *IEEE Trans. Ultrason. Ferroelectr. Freq. Control* **55**(12), 2692–2702 (2008).
- <sup>25</sup>X. Zhao and T. Gang, “Nonparaxial multi-Gaussian beam models and measurement models for phased array transducers,” *Ultrasonics* **49**(1), 126–130 (2009).
- <sup>26</sup>D. Huang and M. A. Breazeale, “A Gaussian finite-element method for description of sound diffraction,” *J. Acoust. Soc. Am.* **106**(4), 1771–1781 (1999).
- <sup>27</sup>W. Liu, P. Ji, and J. Yang, “Development of a simple and accurate approximation method for the Gaussian beam expansion technique,” *J. Acoust. Soc. Am.* **123**(5), 3516 (2008).
- <sup>28</sup>D. Olszewski and K. Linhard, “Highly directional multi-beam audio loudspeaker,” in *Ninth International Conference on Spoken Language Processing* (Curran Associates, Inc., 2006), pp. 2630–2633.
- <sup>29</sup>Y. Sugabayashi, S. Kurimoto, D. Ikefujii, M. Morise, and T. Nishiura, “Three-dimensional acoustic sound field reproduction based on hybrid combination of multiple parametric loudspeakers and electrodynamic subwoofer,” *Appl. Acoust.* **73**(12), 1282–1288 (2012).
- <sup>30</sup>C. Shi, R. Bai, J. Gou, and J. Liang, “Multi-beam design method for a steerable parametric array loudspeaker,” in *2020 Asia-Pacific Signal and Information Processing Association Annual Summit and Conference (APSIPA ASC)* (IEEE, 2020), pp. 416–420.
- <sup>31</sup>J. Zhong, R. Kirby, M. Karimi, and H. Zou, “A cylindrical expansion of the audio sound for a steerable parametric array loudspeaker,” *J. Acoust. Soc. Am.* **150**(5), 3797–3806 (2021).
- <sup>32</sup>J. Zhong, R. Kirby, M. Karimi, and H. Zou, “A spherical wave expansion for a steerable parametric array loudspeaker using zernike polynomials,” *J. Acoust. Soc. Am.* **152**(4), 2296–2308 (2022).